

Fully 4D list-mode reconstruction applied to respiratory-gated PET scans

N Grotus^{1,2,3}, A J Reader⁴, S Stute³, J C Rosenwald¹, P Giraud^{1,5}
and I Buvat³

¹ Institut Curie, Paris, France

² Philips Healthcare, Suresnes, France

³ IMNC, IN2P3, UMR 8165 CNRS—Paris 7 and Paris 11 Universities, Orsay, France

⁴ Brain Imaging Centre, Montreal Neurological Institute, Montreal, Canada

⁵ Hôpital Européen Georges Pompidou, Paris, France

E-mail: grotus@imnc.in2p3.fr

Received 14 October 2008, in final form 26 January 2009

Published 25 February 2009

Online at stacks.iop.org/PMB/54/1705

Abstract

¹⁸F-fluoro-deoxy-glucose (¹⁸F-FDG) positron emission tomography (PET) is one of the most sensitive and specific imaging modalities for the diagnosis of non-small cell lung cancer. A drawback of PET is that it requires several minutes of acquisition per bed position, which results in images being affected by respiratory blur. Respiratory gating techniques have been developed to deal with respiratory motion in the PET images. However, these techniques considerably increase the level of noise in the reconstructed images unless the acquisition time is increased. The aim of this paper is to evaluate a four-dimensional (4D) image reconstruction algorithm that combines the acquired events in all the gates whilst preserving the motion deblurring. This algorithm was compared to classic ordered subset expectation maximization (OSEM) reconstruction of gated and non-gated images, and to temporal filtering of gated images reconstructed with OSEM. Two datasets were used for comparing the different reconstruction approaches: one involving the NEMA IEC/2001 body phantom in motion, the other obtained using Monte-Carlo simulations of the NCAT breathing phantom. Results show that 4D reconstruction reaches a similar performance in terms of the signal-to-noise ratio (SNR) as non-gated reconstruction whilst preserving the motion deblurring. In particular, 4D reconstruction improves the SNR compared to respiratory-gated images reconstructed with the OSEM algorithm. Temporal filtering of the OSEM-reconstructed images helps improve the SNR, but does not achieve the same performance as 4D reconstruction. 4D reconstruction of respiratory-gated images thus appears as a promising tool to reach the same performance in terms of the SNR as non-gated acquisitions while reducing the motion blur, without increasing the acquisition time.

(Some figures in this article are in colour only in the electronic version)

1. Introduction

^{18}F -fluoro-deoxy-glucose (^{18}F -FDG) positron emission tomography (PET) has become one of the most useful imaging modalities for non-small cell lung cancer (NSCLC) diagnosis and staging because of its high sensitivity and specificity (Acker and Burrell 2005, Gould *et al* 2001, Marom *et al* 1999). However, breathing motion reduces the accuracy of NSCLC PET: the blur introduced by motion increases the apparent size of the moving organs or tumors and decreases their apparent uptake on PET images (Boucher *et al* 2004, Livieratos *et al* 2006, Nehmeh *et al* 2002a, 2002b). It can also reduce small lesion detection in PET images (Pevsner *et al* 2005). Furthermore, modern PET systems are now combined with computed tomography (CT) scanners making faster images that are also influenced by respiratory motion. The CT images are used to correct the PET images for photon attenuation and possibly scatter. There is therefore a crucial need for a good registration between CT and PET scans. Efforts are currently made to handle breathing motion in both scans in order to minimize the misregistration between them and to minimize quantification errors (Erdi *et al* 2004, Goerres *et al* 2002a, 2002b, 2003, Nagel *et al* 2006, Pan *et al* 2005).

Even though techniques have been proposed to reduce PET–CT artifacts due to breathing without using respiratory gating (El Naqa *et al* 2006, Pan *et al* 2005), it is becoming a must-use tool to address the respiratory motion problem in PET–CT scans. It has already been shown that respiratory gating of PET–CT scans helps reduce the blur and improve the recovery of the lesion size and uptake (Nehmeh *et al* 2002b, 2003, 2004a, 2004b, Visvikis *et al* 2004, Wolthaus *et al* 2005). However, to retain an appropriate signal-to-noise ratio (SNR) in the gated images, the total number of coincidences detected with the PET scanner needs to be increased by a factor equal to the number of gates (typically 8 or 10). As a consequence, the acquisition time has to be significantly increased (Nehmeh *et al* 2002b, Visvikis *et al* 2004). A way to avoid this increase in PET acquisition duration is to combine the gated frames during or after reconstruction, usually using registration techniques (Dawood *et al* 2006, Lamare *et al* 2007a, 2007b, Livieratos *et al* 2005).

The purpose of this work is to adapt a four-dimensional (4D) image reconstruction algorithm (Reader *et al* 2006, Grotus *et al* 2007) to respiratory-gated list-mode PET data without requiring any information regarding the deformation field due to breathing (which is usually needed with registration techniques). The aim is to determine whether 4D reconstruction can help improve the SNR in the gated images whilst preserving motion deblurring.

2. Materials and methods

2.1. NEMA IEC body phantom acquisition

The NEMA IEC/2001 body phantom was used, including six hot spheres (10, 13, 17, 22, 28, 37 mm in diameter, sphere-to-background activity ratio of 4). The centers of the spheres were all in the same plane and located at 7 cm from the phantom lid. A cold cylinder (51 mm diameter and 180 mm long) was also inserted on the central axis of the phantom. The background of the phantom was filled with 74 MBq (2 mCi) ^{18}F -FDG in water.

The phantom was placed on a moving platform (figure 1). The phantom moved linearly on a ramp placed on the couch of the scanner with a period of 5 s. The amplitudes of the movement were approximately 3.5 cm and 0.5 cm in the axial and vertical directions, respectively.

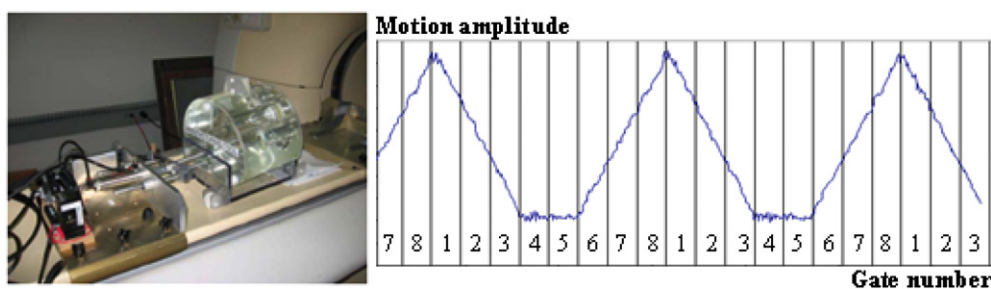


Figure 1. Left: the NEMA IEC body phantom placed on a moving platform. Right: the respiratory signal as recorded by the Varian RPM device. The numbers correspond to the 8 gates obtained by equally splitting the time interval between 2 maxima.



Figure 2. Coronal view of the activity map used for gate 1 of the Monte-Carlo simulations, where the gray levels represent different activity concentrations. The dimensions of the phantom are 188 mm in the axial direction and $576 \times 576 \text{ mm}^2$ in the transaxial direction.

PET data were collected on a Philips Gemini GXL PET-CT scanner. A 20 min list-mode acquisition was performed and the vertical movement of the phantom was recorded with the real-time position management (RPM) device (Varian Medical Systems). In addition, the RPM system sent trigger information to the PET-CT scanner. This trigger is set on the RPM interface and corresponds to a user-defined level of the respiratory signal. The trigger signal is then written in the list-mode file in order to synchronize the respiratory trace with the recorded PET coincidences.

Eight gates were defined by equally dividing the respiration cycle between each maximum of the curve (figure 1), making the eight resulting time bins of the same duration. PET events were then tagged with the corresponding gate number.

2.2. NCAT phantom simulation

The NCAT phantom (Segars *et al* 2001) was used to simulate the realistic human anatomy (figure 2) and the deformation of the organs around the lungs during breathing. The period of the respiratory cycle was set to 4 s. Eight gates were used for the generation of the activity and attenuation maps of the NCAT phantom, where gate 1 corresponded to the end-expiration phase and gate 5 to the end-inspiration phase. Four spherical lesions of diameter 2.5 cm were placed in the right lung. The tumor-to-normal tissue contrast was set to 4. The activity concentration in the lungs was 1 kBq ml^{-1} . The displacements of the four lesions are shown in table 1.

A Monte-Carlo simulation of the PET acquisition of the NCAT phantom was performed with GATE (Jan *et al* 2004). The Philips Gemini GXL geometry was modeled based on

Table 1. Displacements of the four tumors in the three directions. L–R: left–right, A–P: anterior–posterior, S–I: superior–inferior, Norm: total spatial displacement.

Tumor #	Maximum displacement in each direction (in mm)			
	L–R	A–P	S–I	Norm
1	1.2	9.6	18.4	20.8
2	2.0	12.1	15.1	19.5
3	1.9	5.7	10.8	12.3
4	1.7	3.3	9.6	10.3

the work by Lamare *et al* (2006). Sixty one million true coincidences were simulated, corresponding approximately to a 6 min scan for a real PET acquisition of the lungs.

2.3. Reconstruction

All the reconstructions implemented in this study are based on the maximum-likelihood expectation maximization (MLEM) algorithm (Shepp and Vardi 1982), and more precisely on the ordered-subset version of this reconstruction (OSEM) (Hudson and Larkin 1994). The basic equation of MLEM is the following:

$$\hat{f}^{k+1} = \frac{\hat{f}^k}{R^T S^T A^T \mathbf{1}} R^T S^T A^T \frac{p}{ASR\hat{f}^k + s + r}, \quad (1)$$

where p is a vector containing the prompt events, \hat{f}^k is the estimate of the image volume at the k th iteration, R is the matrix that transforms the image f into the measurement space, S is the matrix containing the inverse of the normalization factors accounting for non-homogeneous responses of the crystals, A is the matrix containing the attenuation coefficients, s and r respectively describe the distribution of the scatter and the random events in the measurement space. The $\mathbf{1}$ in the denominator of equation (1) is a vector that contains a value of one in each element.

In list-mode reconstruction, the subsets used in OSEM are defined by equally splitting the list-mode file into the desired number of subsets (Reader *et al* 2002).

The reconstructed voxel size was $4 \times 4 \times 4 \text{ mm}^3$.

For the NEMA phantom, the scatter distribution was estimated using the single scatter simulation (Accorsi *et al* 2004, Ollinger 1996, Werling *et al* 2002). A low-noise estimate of the random coincidences was obtained from a delayed window for the 20 min acquisition. It was then scaled down to obtain an estimate appropriate for the 2 min acquisitions used for the data analysis (see section 2.4.1). The attenuation map was obtained by segmenting the CT images in two compartments: regions with Hounsfield units (HU) between -1000 and -220 were set to $\mu = 0 \text{ cm}^{-1}$ while regions with HU over -220 were set to $\mu = 0.096 \text{ cm}^{-1}$. For each line of response j , the attenuation coefficient of matrix A was calculated as follows:

$$a_j = \int_{-\infty}^{+\infty} \exp(-\mu(x)x) dx, \quad (2)$$

where x is the integration variable along the line of response.

For the NCAT phantom, only true coincidences were reconstructed (s and r were thus empty vectors). The attenuation correction was performed using the attenuation map used for the GATE simulation. As the detection chain was ideal in the simulation, the matrix S

was approximated by the identity matrix, assuming ideal crystals but neglecting efficiency variations as a function of the angle of incidence of each LOR.

For both phantom datasets and for the reconstructions using respiratory gating, all the corrections mentioned above were performed using the data corresponding to the reconstructed gate. The matrix A and vectors s and r in equation (1) are thus different for every gate, while S and R are invariant for all gates. For the non-gated reconstruction, the attenuation correction was performed using the average attenuation map over all the gates.

For computation efficiency reasons, equation (1) was simplified by defining a vector d equal to $S^T A^T I$ (also equal to $AS I$), leading to the following implemented equation:

$$\hat{f}^{k+1} = \frac{\hat{f}^k}{R^T d} R^T \frac{P}{R \hat{f}^k + \frac{s+r}{d}}. \quad (3)$$

Four reconstruction protocols were derived from the OSEM algorithm and compared as follows:

- (1) 4D-reconstruction (4DR): the 4D joint-estimation algorithm (Reader *et al* 2006) we considered assumes that the time course $f(i, t)$ of each voxel i (an 8-value vector when using eight respiratory gates) can be written as a linear combination of a small number N of temporal basis functions. The corresponding equation is

$$f(i, t) = \sum_{n=1}^N b_n(t) w_n(i). \quad (4)$$

Only the N basis functions $b_n(t)$ and the weights of each voxel $w_n(i)$ for these basis functions need to be estimated, significantly reducing the number of unknowns. In addition, as the basis functions span the whole temporal range, the method intrinsically includes some temporal regularization. Basis functions and weight images are updated iteratively as in an OSEM technique using

$$\hat{w}^{k+1} = \frac{\hat{w}^k}{C_b^T R^T d} C_b^T R^T \frac{P}{R C_b \hat{w}^k + \frac{s+r}{d}} \quad (5)$$

$$\hat{b}^{k+1} = \frac{\hat{b}^k}{C_w^T R^T d} C_w^T R^T \frac{P}{R C_w \hat{b}^k + \frac{s+r}{d}}, \quad (6)$$

where p is a vector containing the prompt events for all gates, s and r are vectors that respectively contain the scatter and random estimates for all gates. The d vector also contains the correction factors for all gates.

C_b and C_w are the matrices used to connect the basis functions b_n and the weight images w_n :

$$C_w b = C_b w = f. \quad (7)$$

The N basis functions $b_n(t)$ are initialized as sinusoids with all sinusoids having the same frequency but different phases. The weight images $w_n(i)$ are initialized as uniform images. Basis functions and weight images contain non-negative numbers only and remain positive or zero at all iterations of the algorithm (see equations (5) and (6)). The weight images and the basis functions are both updated for every subset by running equations (5) and (6) successively. For a particular subset, equation (5) is first run to update the weight images w , then equation (7) is used to get the matrix C_w and finally equation (6) yields an updated C_w matrix to get the new estimate for the b vector of basis functions. Then the same procedure is repeated using the next subset. The convergence speed of the 4D

Table 2. Parameters used for the four reconstruction protocols.

	4DR (1)		IFR and TF-IFR (2, 3)		NGR (4)	
	Iterations	Subsets	Iterations	Subsets	Iterations	Subsets
NEMA IEC body phantom	Up to 40	10	Up to 40	10	Up to 40	80
NCAT phantom	Up to 80	10	Up to 80	10	Up to 80	80

algorithm depends on the number of basis functions and how they are initialized (Reader *et al* 2006).

A number $N = 2$ to 8 basis functions were used for the 4D reconstructions of the NEMA acquisition and for the NCAT simulation. The numbers of iterations and subsets used for the 4D reconstruction and for the two datasets are summarized in table 2.

The influence of the number N of basis functions was studied using a noise-free dataset extracted from the activity map used for the NCAT simulation. A cubic ($6 \times 6 \times 6 = 216$ voxels) volume of interest located at the edge of a tumor was considered to investigate the motion recovery in that phantom, as a function of N . The time-activity curves of these 216 voxels were calculated, as well as the mean activity in each voxel over time and associated standard deviation. The 216 voxels were sorted in standard deviation ascending order when plotting the results, to distinguish between voxels with small or large variations in activity content along time, corresponding to voxels weakly or largely affected by breathing motion, respectively. For each voxel, the mean relative error in activity estimate over the 8 gates was calculated for the time-activity curve after 100 iterations of the 4D algorithm using

$$\langle v \rangle = \frac{1}{T} \sum_{t=1}^T \frac{|v_{\text{est}}(t) - v_{\text{true}}(t)|}{v_{\text{true}}(t)}, \quad (8)$$

where $T = 8$ is the number of gates, v_{true} is the true time-activity curve of the voxels and v_{est} is the time-activity curve estimated by the 4D algorithm.

The true maximum amplitude of the time-activity curve for each of the 216 pixels was also calculated and compared to the maximum amplitude obtained using the time-activity curves estimated by the 4D algorithm.

- (2) Independent-frame reconstruction (IFR): each gate was reconstructed using OSEM. The parameters of the reconstruction are given in table 2.
- (3) Independent-frame reconstruction followed by temporal filtering (TF-IFR): OSEM reconstruction was used as in the IFR method, and the resulting set of gated images was filtered along time using a Gaussian kernel with a standard deviation varying from 0.1 to 3.9 (in gate units). The parameters of the reconstruction are given in table 2.
- (4) Non-gated reconstruction (NGR): each acquisition was reconstructed without respiratory gating, using OSEM. The parameters of the reconstruction are given in table 2.

For each reconstruction protocol, no spatial post-filtering of the images was performed.

2.4. Data analysis

2.4.1. NEMA IEC body phantom. To obtain the multiple acquisition datasets needed to properly assess noise in the reconstructed images, the list-mode file was split into ten 2 min acquisitions.

For each gate, the mean image and the standard-deviation image over the ten 2 min replicates were calculated for the four reconstruction protocols. The signal-to-noise ratio (SNR) was measured in a region of interest (ROI) manually drawn in the background of the phantom, far from the phantom rim and from the spheres, to avoid spill-in from other compartments. The SNR was defined as the ratio of the mean value in this ROI measured on the mean image to the mean value in this ROI measured on the standard-deviation image. The SNR was calculated for each gate. Contrast was measured as the ratio of the mean pixel value in the background of the phantom to the mean pixel value in the cold cylinder (BCR). The ROIs used for the background were the same as for the SNR measurement. For the cold cylinder, ROIs were also manually drawn on each gate, well inside the actual cylinder edges, to reduce spill-in from surrounding activity. The SNR and BCR were calculated for each iteration. A sphere-to-background activity ratio was calculated as the ratio of the mean pixel value in the spheres to the mean pixel value in the background measured in the ROI previously defined. The ROIs used for the spheres had the same volume as the spheres. The positions of these spherical ROIs were set by maximizing the mean pixel value on the images reconstructed using the independent reconstruction. To assess the deblurring effect of the 4D reconstruction, the position of the center of mass of the 37 mm diameter sphere was calculated for each gate for the same BCR on every set of reconstructed images. The mean relative error on the position of this center of mass over the 8 gates (relative to the position of the sphere on the CT images) was calculated in the axial direction using

$$\langle z \rangle = \frac{1}{T} \sum_{t=1}^T \frac{|z_{\text{est}}(t) - z_{\text{CT}}(t)|}{z_{\text{CT}}(t)}, \quad (9)$$

where $T = 8$ is the number of gates, z_{CT} is the axial position of the sphere on the CT images and z_{est} is the axial position of the center of mass of the sphere on the reconstructed PET images.

The axial direction was chosen because the motion of the sphere is maximal in this direction (see section 2.1). The SNR, BCR and center of mass positions were calculated for each reconstruction protocol and for each iteration number.

2.4.2. NCAT phantom. The signal-to-noise ratio (SNR) was measured in an ROI placed in the soft tissue. The SNR was calculated as the ratio of the mean value to the standard deviation value in this ROI. A contrast index was calculated as the ratio of the mean value in the most mobile tumor (lesion 1 in table 1) to the mean value in the soft tissue (ideal value = 4). The mean value in the tumor was measured using the exact tumor contours used in the Monte-Carlo simulation. The centers of mass of the lesions were also calculated to evaluate the recovery of the tumor positions. The mean relative errors on the positions of these centers of mass over the 8 gates (relative to the position of the tumors on the activity map used for the GATE simulation) were calculated in the three directions using

$$\langle X \rangle = \frac{1}{T} \sum_{t=1}^T \frac{|X_{\text{est}}(t) - X_{\text{act_map}}(t)|}{X_{\text{act_map}}(t)}, \quad (10)$$

where $T = 8$ is the number of gates, $X_{\text{act_map}}$ is the coordinate of the tumors on the activity map used for the GATE simulation and X_{est} is the coordinate of the center of mass of the tumors on the reconstructed PET images. The SNR, contrast and center of mass positions were calculated for each reconstruction protocol and for each iteration number.

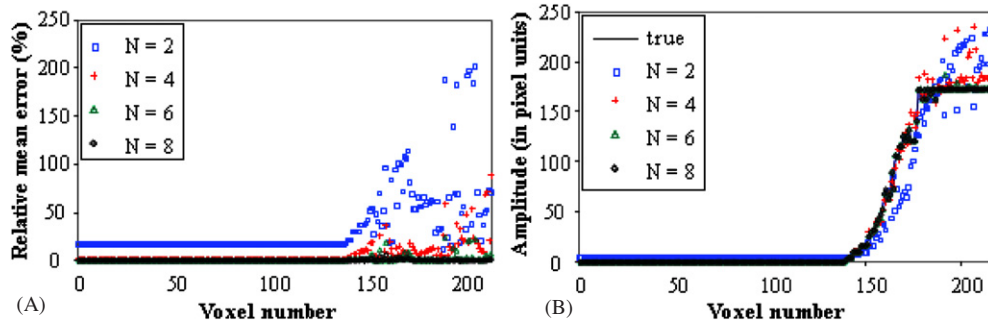


Figure 3. (A) Mean error (ν) in activity estimates for the 216 time-activity curves of the NCAT phantom ROI as a function of the number N of basis functions. (B) Maximum amplitude of the time-activity curve of the 216 pixels as estimated by the 4D algorithm compared to the true amplitude of these time courses. The voxels were numbered by sorting them by increasing the standard deviation of the corresponding voxel time-activity curve, to distinguish between voxels with small or large variations in activity content along time, corresponding to voxels weakly or largely affected by breathing motion, respectively. For instance, voxels 0 to 139 were not affected by motion at all, while voxel 216 was the most affected by motion.

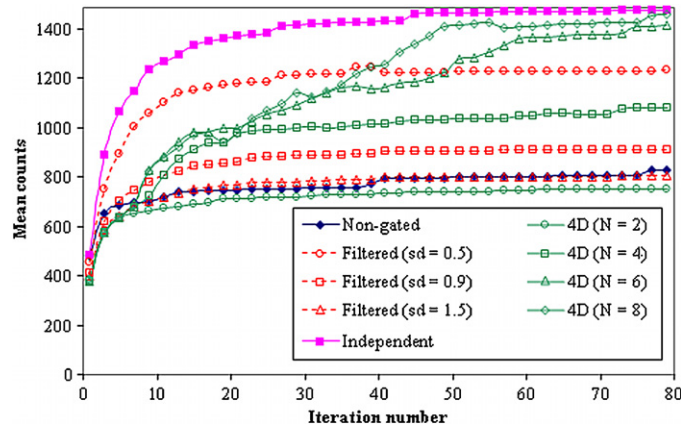


Figure 4. Average number of counts in lesion 1 of the NCAT phantom for gate 7 and for all the reconstruction protocols.

3. Results

3.1. Validation of the 4D reconstruction model

3.1.1. Noise-free dataset. The mean errors (ν) in activity estimates over the 8 gates measured in the 216 voxels of the NCAT phantom activity map (see section 2.2 and equation (8)) are shown in figure 3(A) for 2, 4, 6 and 8 basis functions. Figure 3(B) shows the maximum amplitudes of the time courses of the 216 pixels estimated by the 4D algorithm.

3.1.2. Noisy data. Figure 4 represents the average number of counts in lesion 1 of the NCAT phantom for gate 7 as a function of the iteration number, for the 4DR using 2, 4, 6 or 8 basis functions. The average value for lesion 1 is decreased by 49%, 27%, 4% and 1% compared to

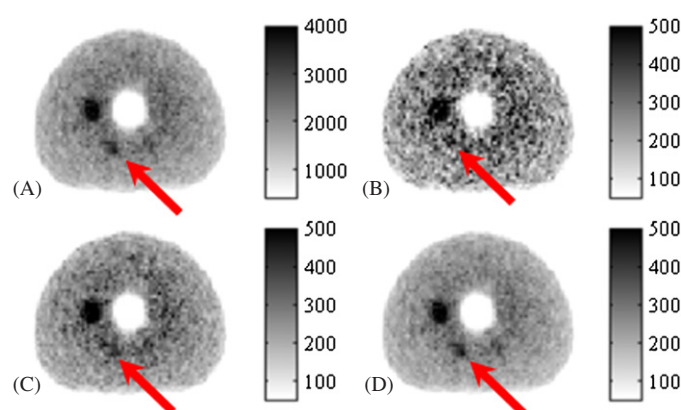


Figure 5. Reconstructed images for gate 7 and a BCR of 4 using the 4 reconstruction protocols. A: NGR, B: IFR, C: TF-IFR with a Gaussian kernel (standard deviation of 0.9), D: 4DR ($N = 6$).

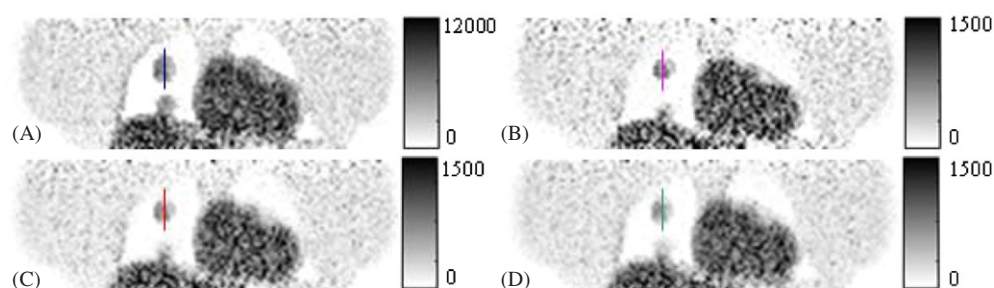


Figure 6. Reconstructed images of the NCAT phantom for gate 3 and a contrast of 2.5 using the four reconstruction protocols. A: NGR, B: IFR, C: TF-IFR with a Gaussian kernel (standard deviation of 0.9), D: 4DR ($N = 6$). The vertical lines indicate the location of the profiles plotted in figure 11.

independent reconstruction when using 2, 4, 6 and 8 basis functions respectively at iteration 80. Overall figures 3 and 4 suggest that $N = 6$ or 8 yields a proper recovery of the activity values in the different time frames but that lower N values might introduce significant biases in activity estimates.

3.2. Reconstructed images

Figures 5 and 6 show the images obtained with the four reconstruction protocols. Based on the previous results (figures 3 and 4), $N = 6$ basis functions were used for the 4D reconstruction. Figures 5 and 6 clearly show the higher level of noise in the gated images reconstructed with independent-frame OSEM (B) than in the non-gated images (A). This is because there are eight times fewer counts in the gated acquisition than in the non-gated one. The level of noise is decreased when using 4D reconstruction (D) or with temporal smoothing of the images reconstructed with the independent-frame OSEM algorithm (C). Figure 5 also shows that the 28 mm diameter sphere (see arrows) almost disappear in the presence of noise with independent-frame OSEM while it clearly appears on images reconstructed with the 4D

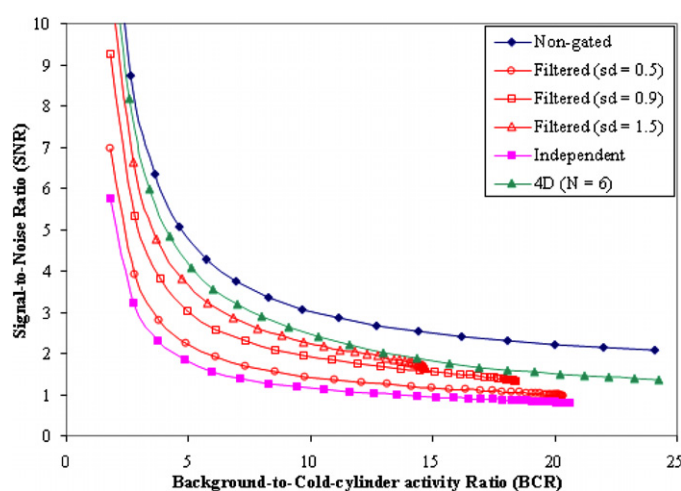


Figure 7. Variation of the signal-to-noise ratio (SNR) against the background-to-cold-cylinder activity ratio (BCR) for gate 2 in the NEMA phantom. Each point of the curves represents a different iteration number in the reconstruction algorithms.

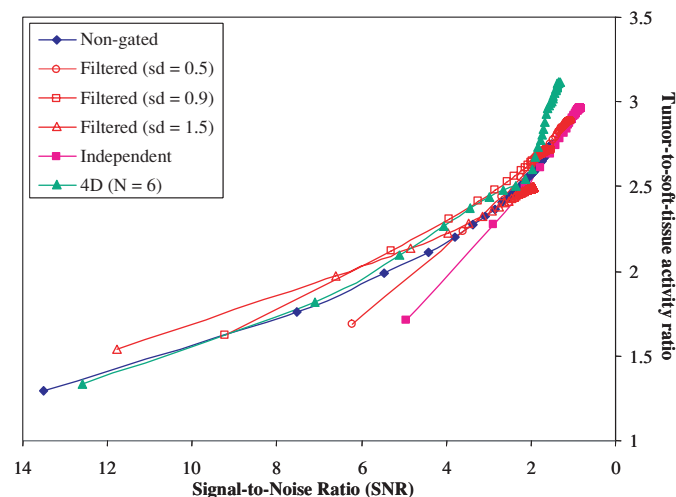


Figure 8. Tumor-to-soft-tissue activity ratio against signal-to-noise ratio averaged over the 8 gates in the NCAT phantom. Each point of the curves represents a different iteration number in the reconstruction algorithms.

reconstruction. Filtered independent reconstruction does not show great improvements in the recovery of this sphere.

3.3. SNR performance

Figures 7 and 8 show the performance of the four reconstruction protocols in terms of signal-to-noise ratio for the NEMA phantom study and the NCAT phantom study, respectively. For the NEMA phantom, for all iterations considered, the SNR is greater when using the 4D reconstruction than when using the independent-frame reconstruction with or without

Table 3. Percent error in quantification in the four largest spheres of the NEMA phantom relative to IFR.

Sphere diameter (in mm)	NGR	TF-IFR (sd = 0.5)	TF-IFR (sd = 0.9)	TF-IFR (sd = 1.5)	4DR ($N = 6$)
17	-32.2	-3.7	-9.9	-15	-11.1
22	-28.5	-3.4	-9.5	-14.9	-10.1
28	-26.1	-2.9	-8.4	-13.6	-7.2
37	-28.3	-2.6	-7.6	-12.5	-4.6
Average	-28.8	-3.2	-8.9	-14.0	-8.3

temporal filtering. For the NCAT phantom, the SNR is greater with 4D reconstruction than with any other reconstruction after ten iterations. The results corresponding to three different standard deviation values for the temporal post-filter are shown for the TF-IFR. With a standard deviation of 0.5, the trade-off between signal-to-noise ratio and contrast is only slightly improved compared to independent reconstruction. This trade-off is further improved when using a standard deviation of 0.9 for the Gaussian kernel. The last standard deviation value of 1.5 illustrates the limited increase of the SNR and the biased contrast when increasing the temporal smoothing.

3.4. Quantification

Table 3 shows the percent difference in the sphere-to-background activity ratio with respect to the sphere-to-background activity ratio obtained on the IFR images, for the four largest spheres of the NEMA phantom and for every reconstruction. These errors were calculated for a BCR of 12. The smallest two spheres were omitted because they could not be seen on any reconstructed images. For all spheres, non-gated reconstruction shows the largest error (-28.8% in average). 4DR with six basis functions shows a mean error of -8.3% while filtered reconstructions yield mean errors of -3.2%, -8.9% and -14% with standard deviations of 0.5, 0.9 and 1.5, respectively.

As mentioned in section 3.1.2, figure 4 represents the average number of counts in lesion 1 of the NCAT phantom for gate 7 as a function of the iteration number. The average counts plotted for the non-gated reconstruction is divided by 8 to match the scale of the gated reconstructions. Independent reconstruction achieves the highest average value. When filtering with Gaussian kernels, the average value at convergence is decreased by 16%, 38% and 45% compared to independent reconstruction at iteration 80 when using standard deviations of 0.5, 0.9 and 1.5, respectively. These values for the standard deviations describe the typical behaviors of the Gaussian filtering. Choosing a standard deviation value of 0.5 yields an activity value in tumor 1 close to that obtained with the IFR. With a standard deviation of 1.5, the activity value in tumor 1 is highly biased and very close to the result of the non-gated reconstruction. Intermediate results are obtained with a standard deviation of 0.9. The average value for lesion 1 obtained with 4DR is decreased by 49%, 27%, 4% and 1% compared to independent reconstruction when using 2, 4, 6 and 8 basis functions respectively at iteration 80. Due to the motion blur in the reconstructed images, the average value obtained with the NGR is decreased by 44% compared to the IFR at iteration 80.

3.5. Motion recovery

Figure 9 shows the axial position of the center of mass $\langle z \rangle$ of the largest sphere in the NEMA phantom as a function of the gate number. As expected, the NGR yields the largest average error (10.6%) on the sphere position along the 8 gates, whereas the independent

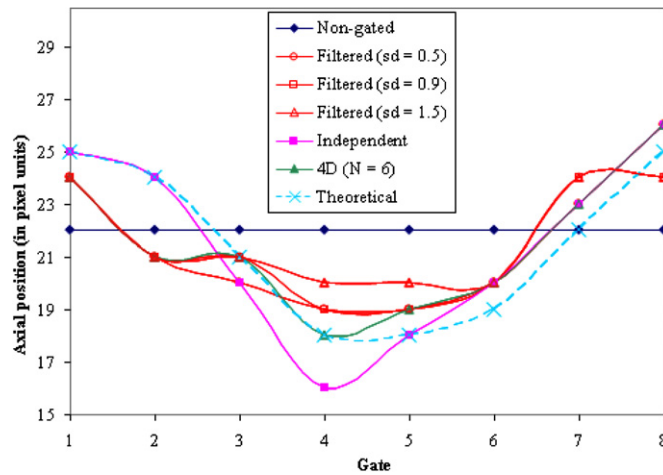


Figure 9. Axial position of the center of mass (z) of the largest sphere of the NEMA phantom in the axial direction as a function of the gate number, and for a BCR of 12.

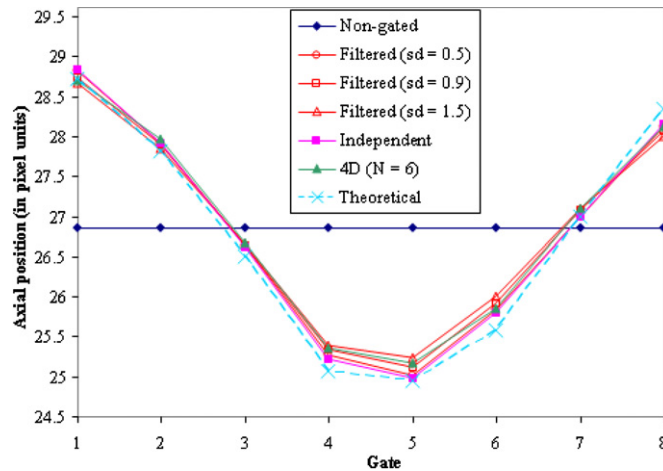


Figure 10. Axial position of the center of mass (X) of lesion 1 of the NCAT phantom in the axial direction on the 8 gates for a SNR of 2.5.

reconstruction shows the smallest error (3.1%). TF-IFR yield mean errors of 5.5%, 5.5% and 6.5% for standard deviation of the smoothing Gaussian kernel of 0.5, 0.9 and 1.5, respectively. Mean errors with 4DR are 5.2%, 5.4%, 4.5% and 3.3% for 2, 4, 6 and 8 basis functions respectively (curves shown for six basis functions only).

Figure 10 shows the axial position of the center of mass (X) of tumor 1 (see table 2 for tumor numbering) in the NCAT phantom as a function of the gate number. The best fit with the theoretical position is found with the IFR. 4DR and TF-IFR show similar performance in terms of tumor position recovery. Table 4 summarizes the errors made on the positions of the centers of mass for all tumors of the NCAT simulation and for all the reconstruction protocols.

Count-profiles through tumor 1 of the NCAT phantom on gate 4 are plotted in figure 11 for the different reconstruction methods. The narrowest profile is obtained for the independent

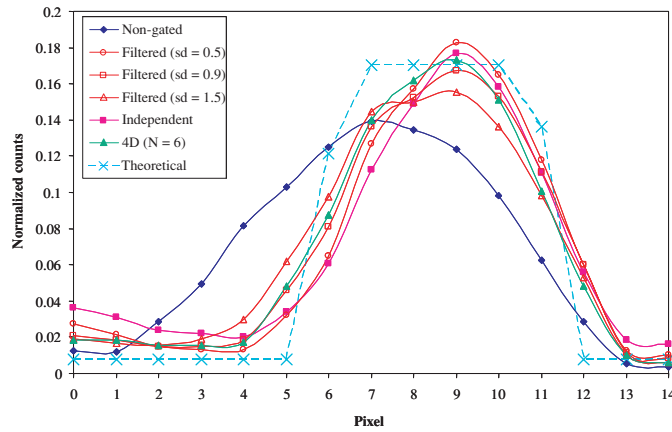


Figure 11. Profiles for the four reconstruction protocols across tumor 2 of the NCAT phantom for gate 4 and for an SNR of 2.5.

Table 4. Percentage error on the center of mass position (X) in the three directions for the four tumors of the NCAT phantom and for all the reconstruction protocols. S-I: superior-inferior, A-P: anterior-posterior, L-R: left-right.

Direction	Tumor #	NGR	IFR	TF-IFR (sd = 0.5)	TF-IFR (sd = 0.9)	TF-IFR (sd = 1.5)	4DR ($N = 6$)
S-I	1	12.0	0.4	0.6	1.1	1.3	1.3
	2	4.6	0.5	0.5	0.7	0.8	0.7
	3	3	0.6	0.6	0.7	0.7	0.7
	4	2.5	1.0	1.0	1.1	1.1	0.9
A-P	1	1.5	0.5	0.6	0.6	0.6	0.6
	2	1.7	0.3	0.3	0.3	0.3	0.4
	3	0.9	0.4	0.4	0.4	0.4	0.4
	4	0.5	0.4	0.4	0.4	0.4	0.4
L-R	1	0.7	0.2	0.2	0.2	0.2	0.2
	2	0.2	0.2	0.2	0.2	0.2	0.2
	3	0.8	0.6	0.6	0.6	0.6	0.6
	4	0.6	0.8	0.8	0.8	0.8	0.8

reconstruction, and has a full width at half maximum (FWHM) of 4.8 pixels. The FWHM of the profile for TF-IFR increases with the standard deviation of the Gaussian filter (respectively 5.0, 5.6, 6.0 pixels for standard deviations of 0.5, 0.9 and 1.5). The FWHM obtained with the 4D reconstruction using six basis functions is 5.2 pixels. The largest profile was obtained with the non-gated reconstruction (FWHM of 7.2 pixels).

4. Discussion

The 4D joint-estimation reconstruction algorithm described in this paper was initially designed in the context of dynamic PET acquisitions, to help estimate the kinetics of the radiotracer uptake (Reader *et al* 2006). The main advantage of this 4D algorithm is that it intrinsically includes some temporal regularization during the reconstruction process by using temporal basis functions. In the context of dynamic PET, it has been shown that the trade-off between

bias and signal-to-noise ratio is better in the 4D-reconstructed images compared to other reconstruction methods.

In this study, we took advantage of the 4D reconstruction principle to increase the SNR in respiratory-gated images. The method uses all the acquired coincidences over all the respiratory cycles to reconstruct the gated data, making it possibly unnecessary to increase the acquisition time for compensating for the fractionation of the data introduced by the respiratory gating technique. We indeed found that by combining all the events recorded at different phases of the respiratory cycles, the SNR is improved in the reconstructed images compared to the images obtained with independent reconstructions of each gate. This is because the 4DR introduces some temporal regularization in the reconstruction process, through the basis functions common to all voxels. The SNR of gated images that are independently reconstructed can actually be increased by temporal filtering along the gates. The temporal filter used in this study was a Gaussian filter. Other types of filters could have been employed such as filters designed in the frequency domain (Kohlmyer *et al* 2007). These filters are more difficult to optimize due to the choice of the cut-off frequency that must be adapted to the respiratory frequency of every patient. We found that when using Gaussian smoothing kernels, the choice of the standard deviation had a high impact on the resulting images. Choosing a low value for the standard deviation (e.g. 0.5) led to only slight improvements of the SNR, while high values for the standard deviation led to biased results in terms of contrast recovery. The results presented here show that using a Gaussian kernel with a standard deviation of 0.9 yielded similar results to 4D reconstruction in terms of tumor motion recovery (figures 9 and 10). However, the use of this Gaussian kernel severely biased the activity estimate in the moving lesions (figure 4).

The 4D reconstruction also involves a critical parameter, namely the number N of basis functions used for the reconstruction. No significant difference was observed between 2 to 8 basis functions in terms of signal-to-noise ratio (result not shown). Regarding motion recovery, increasing the number of basis functions yielded better motion recovery (section 3.5). 4D reconstruction introduced a small bias (4% with six basis functions for the NCAT phantom) in activity estimates compared to independent reconstruction (figure 4), but when the number of basis functions was greater than 4, this bias was smaller than that obtained with independent reconstruction followed by temporal filtering with a standard deviation of the Gaussian kernel of 0.5. Overall, 4D reconstruction can thus yield a better trade-off between SNR and bias in the estimates of activity in moving tumors than filtered-independent reconstruction (figures 4–8).

Compared to other techniques for respiratory motion compensation in PET images (Dawood *et al* 2006, Lamare *et al* 2007a, 2007b), the 4D reconstruction described in this paper does not need any estimate of the deformation map between gates, and does not involve any image registration. This can be viewed as an advantage. For example, when the deformation field is derived from the CT, the relevance of using this field for PET motion correction (Lamare *et al* 2007b) is questionable, given the intra-patient variability of breathing motion (Kinahan *et al* 2007). Deriving the motion field from the PET data themselves might appear more appropriate (Livieratos *et al* 2005, Thorndyke *et al* 2006) but a precise estimate of the motion field in this case is challenging given the modest spatial resolution and the high noise level of the gated PET images. The 4D reconstruction approach does not involve any assumption regarding the deformation field during breathing, and does not assume rigid or affine motion for instance. Therefore, the spatial consistency of the ‘hidden’ deformation field cannot be checked or constrained. However, given that 4D reconstruction yields all the images corresponding to each gate, this makes it possible to subsequently estimate the deformation field associated with patient breathing in the PET scan. A mechanism deriving the motion

field from the reconstructed images and checking its consistency might be worth designing, which would ensure that the images corresponding to the different gates are consistent both in time (as the time course in each voxel is constrained by the 4D model) and space.

As all the reconstructions considered in this study are based on a list-mode collection of the PET events, the computational time required by the 4D reconstruction is the same as that of the independent reconstruction of all gated frames. It is also identical to the time required for the reconstruction of the ungated data. This is because the most time-consuming steps are the forward and backward projections. The number of projection/backprojection operations depends only on the number of events in the list-mode file and the number of iterations used. Obviously, the reconstruction of only one gate would take eight times less time than every other technique but as shown in this paper, this is at the expense of a large decrease in signal-to-noise ratio.

Even if the 4D reconstruction we considered is based on list-mode PET data, a similar approach could be implemented in sinogram format as long as sinograms corresponding to each gate are available. When using 8 gates for instance, the reconstruction would thus handle 8 sinograms instead of one list-mode file.

Monte-Carlo simulations of the NCAT phantom allowed us to perform a careful evaluation of the different reconstruction protocols for known activity maps and breathing pattern. Such detailed investigation would not have been possible using real data. We still used a real dataset of the NEMA IEC body phantom to prove the feasibility of the practical implementation of the 4D reconstruction, even if the motion implemented when using this phantom was very simple compared to what could be expected in a real patient.

5. Conclusion

We introduced an original reconstruction scheme for respiratory-gated PET-CT acquisitions, based on a 4D list-mode reconstruction algorithm. We showed that such 4D reconstruction applied on respiratory-gated images improves the signal-to-noise ratio in the PET images compared to the images obtained with independent-gate reconstruction. Temporal post-filtering of independently reconstructed images also improves the signal-to-noise ratio but reduces the activity recovery in small lesions to a greater extent than 4D reconstruction. Overall, 4D reconstruction appears to be a promising approach to make the most of respiratory-gated PET acquisitions, without the need to lengthen the scan duration nor to estimate the organ motion between gates.

Acknowledgments

The authors would like to thank Piotr Maniawski, Ralph Brinks and Thomas Beyer from Philips Healthcare for their assistance in the realization of this study.

References

- Accorsi R, Adam L E, Werner M E and Karp J S 2004 Optimization of a fully 3D single scatter simulation algorithm for 3D PET *Phys. Med. Biol.* **49** 2577–98
- Acker M R and Burrell S C 2005 Utility of 18F-FDG PET in evaluating cancers of lung *J. Nucl. Med. Technol.* **33** 69–74
- Boucher L, Rodrigue S, Lecomte R and Benard F 2004 Respiratory gating for three-dimensional PET of the thorax: feasibility and initial results *J. Nucl. Med.* **45** 214–9
- Dawood M, Lang N, Jiang X and Schafers K P 2006 Lung motion correction on respiratory-gated 3D PET/CT images *IEEE Trans. Med. Imaging* **25** 476–85

- El Naqa I, Low D A, Bradley J D, Vicic M and Deasy J O 2006 Deblurring of breathing motion artifacts in thoracic PET images by deconvolution methods *Med. Phys.* **33** 3587–600
- Erdi Y E *et al* 2004 The CT motion quantitation of lung lesions and its impact on PET-measured SUVs *J. Nucl. Med.* **45** 1287–92
- Goerres G W, Burger C, Kamel E, Seifert B, Kaim A H, Buck A, Buehler T C and Von Schulthess G K 2003 Respiration-induced attenuation artifact at PET/CT: technical considerations *Radiology* **226** 906–10
- Goerres G W, Kamel E, Heidelberg T N, Schwitter M R, Burger C and von Schulthess G K 2002a PET–CT image co-registration in the thorax: influence of respiration *Eur. J. Nucl. Med. Mol. Imaging* **29** 351–60
- Goerres G W, Kamel E, Seifert B, Burger C, Buck A, Hany T F and Von Schulthess G K 2002b Accuracy of image coregistration of pulmonary lesions in patients with non-small cell lung cancer using an integrated PET/CT system *J. Nucl. Med.* **43** 1469–75
- Gould M K, Maclean C C, Kuschner W G, Rydzak C E and Owens D K 2001 Accuracy of positron emission tomography for diagnosis of pulmonary nodules and mass lesions: a meta-analysis *JAMA* **285** 914–24
- Grotus N, Reader A J, Brinks R, Maniawski P, Servois V, Rosenwald J-C, Giraud P and Buvat I 2007 Fully 4D reconstruction applied to respiratory-gated PET acquisitions *Proc. Conf. IEEE Nucl. Sci. Symp. and Medical Imaging* vol 6, pp 4401–5
- Hudson H M and Larkin R S 1994 Accelerated image reconstruction using ordered subsets of projection data *IEEE Trans. Med. Imaging* **13** 601–9
- Jan S *et al* 2004 GATE: a simulation toolkit for PET and SPECT *Phys. Med. Biol.* **49** 4543–61
- Kinahan P, Wollenweber S, Alessio A, Kohlmyer S, MacDonald L, Lewellen T and Ganin A 2007 Impact of respiration variability on respiratory-gated whole-body PET/CT imaging *J. Nucl. Med.* **48** 196P Meeting Abstracts
- Kohlmyer S, Alessio A, Kinahan P and Fessler J 2007 4D PET temporal smoothing with respiratory induced Fourier filter (RIFF) *J. Nucl. Med.* **48** 197P Meeting Abstracts
- Lamare F, Cresson T, Savean J, Cheze Le Rest C, Reader A J and Visvikis D 2007a Respiratory motion correction for PET oncology applications using affine transformation of list-mode data *Phys. Med. Biol.* **52** 121–40
- Lamare F, Ledesma Carbayo M J, Cresson T, Kontaxakis G, Santos A, Le Rest C C, Reader A J and Visvikis D 2007b List-mode-based reconstruction for respiratory motion correction in PET using non-rigid body transformations *Phys. Med. Biol.* **52** 5187–204
- Lamare F, Turzo A, Bizais Y, Le Rest C C and Visvikis D 2006 Validation of a Monte Carlo simulation of the Philips Allegro/GEMINI PET systems using GATE *Phys. Med. Biol.* **51** 943–62
- Livieratos L, Rajappan K, Stegger L, Schafers K, Bailey D L and Camici P G 2006 Respiratory gating of cardiac PET data in list-mode acquisition *Eur. J. Nucl. Med. Mol. Imaging* **33** 584–8
- Livieratos L, Stegger L, Bloomfield P M, Schafers K, Bailey D L and Camici P G 2005 Rigid-body transformation of list-mode projection data for respiratory motion correction in cardiac PET *Phys. Med. Biol.* **50** 3313–22
- Marom E M, McAdams H P, Erasmus J J, Goodman P C, Culhane D K, Coleman R E, Herndon J E and Patz E F Jr 1999 Staging non-small cell lung cancer with whole-body PET *Radiology* **212** 803–9
- Nagel C C, Bosmans G, Dekker A L, Ollers M C, De Ruyscher D K, Lambin P, Minken A W, Lang N and Schafers K P 2006 Phased attenuation correction in respiration correlated computed tomography/positron emitted tomography *Med. Phys.* **33** 1840–7
- Nehmeh S A *et al* 2002a Effect of respiratory gating on reducing lung motion artifacts in PET imaging of lung cancer *Med. Phys.* **29** 366–71
- Nehmeh S A *et al* 2004a Quantitation of respiratory motion during 4D-PET/CT acquisition *Med. Phys.* **31** 1333–8
- Nehmeh S A *et al* 2004b Four-dimensional (4D) PET/CT imaging of the thorax *Med. Phys.* **31** 3179–86
- Nehmeh S A, Erdi Y E, Ling C C, Rosenzweig K E, Schoder H, Larson S M, Macapinlac H A, Squire O D and Humm J L 2002b Effect of respiratory gating on quantifying PET images of lung cancer *J. Nucl. Med.* **43** 876–81
- Nehmeh S A, Erdi Y E, Rosenzweig K E, Schoder H, Larson S M, Squire O D and Humm J L 2003 Reduction of respiratory motion artifacts in PET imaging of lung cancer by respiratory correlated dynamic PET: methodology and comparison with respiratory gated PET *J. Nucl. Med.* **44** 1644–8
- Ollinger J M 1996 Model-based scatter correction for fully 3D PET *Phys. Med. Biol.* **41** 153–76
- Pan T, Mawlawi O, Nehmeh S A, Erdi Y E, Luo D, Liu H H, Castillo R, Mohan R, Liao Z and Macapinlac H A 2005 Attenuation correction of PET images with respiration-averaged CT images in PET/CT *J. Nucl. Med.* **46** 1481–7
- Pevsner A, Nehmeh S A, Humm J L, Mageras G S and Erdi Y E 2005 Effect of motion on tracer activity determination in CT attenuation corrected PET images: a lung phantom study *Med. Phys.* **32** 2358–62
- Reader A J, Ally S, Bakatselos F, Manavaki R, Walledge R J, Jeavons A P, Julyan P J, Zhao S, Hastings D L and Zweit J 2002 One-pass list-mode EM algorithm for high-resolution 3D PET image reconstruction into large arrays *IEEE Trans. Nucl. Sci.* **49** 693–9
- Reader A J, Sureau F C, Comtat C, Trebossen R and Buvat I 2006 Joint estimation of dynamic PET images and temporal basis functions using fully 4D ML-EM *Phys. Med. Biol.* **51** 5455–74

- Segars W P, Lalush D S and Tsui B M W 2001 Modeling respiratory mechanics in the MCAT and spline-based MCAT phantoms *IEEE Trans. Nucl. Sci.* **48** 89–97
- Shepp L A and Vardi Y 1982 Maximum likelihood reconstruction for emission tomography *IEEE Trans. Med. Imaging* **1** 113–22
- Thorndyke B, Schreibmann E, Koong A and Xing L 2006 Reducing respiratory motion artifacts in positron emission tomography through retrospective stacking *Med. Phys.* **33** 2632–41
- Visvikis D, Barret O, Fryer T D, Lamare F, Turzo A, Bizais Y and Le Rest C C 2004 Evaluation of respiratory motion effects in comparison with other parameters affecting PET image quality *Proc. Conf. IEEE Nucl. Sci. Symp. and Medical Imaging* vol 6, pp 3668–72
- Werling A, Bublitz O, Doll J, Adam L E and Brix G 2002 Fast implementation of the single scatter simulation algorithm and its use in iterative image reconstruction of PET data *Phys. Med. Biol.* **47** 2947–60
- Wolthaus J W, van Herk M, Muller S H, Belderbos J S, Lebesque J V, de Bois J A, Rossi M M and Damen E M 2005 Fusion of respiration-correlated PET and CT scans: correlated lung tumor motion in anatomical and functional scans *Phys. Med. Biol.* **50** 1569–83